

The Pseudo Evolution of Galaxy-Cluster Masses and Its Connection to Mass Density Profile

MASATO SHIRASAKI¹

¹*National Astronomical Observatory of Japan, Mitaka, Tokyo 181-8588, Japan*

Submitted to ApJ

ABSTRACT

A mass of dark matter halo is commonly defined as the spherical over-density (SO) mass with respect to a reference density, whereas the time evolution of an SO mass can be affected by the redshift evolution of the reference density as well as the physical mass accretion around halos. In this study, we directly measure the amount of pseudo evolution of the SO masses of cluster-sized halos by the changes in the reference density from a time series of N -body simulations for the first time. We find that the $52 \pm 19\%$ difference in the virial SO masses between $z = 0$ and 1 can be accounted for by the pseudo evolution of clusters with a virial mass of $10^{14} h^{-1} M_{\odot}$ at $z = 0$. The amount of pseudo evolution is found to be correlated with the age and density environment of a galaxy cluster. The stacked mass density profiles of cluster-sized halos with a greater amount of pseudo evolution in the SO mass shows the higher concentration *and* greater linear bias parameter that is a counter-example of the known secondary halo bias due to concentration on the scale of clusters. We discuss how more concentrated clusters can show larger clustering amplitudes than their less concentrated counterparts and argue that the presence of rich filamentary structures plays a critical role in determining the linear halo bias of galaxy clusters.

Keywords: cosmology: large-scale structure of universe — galaxies: clusters — methods: numerical

1. INTRODUCTION

Galaxy clusters are known to be the largest self-bound objects in the universe, and the statistical properties of these clusters are of significant importance in modern cosmology. The number density of galaxy clusters as a function of mass is expected to be sensitive to the gravitational growth in linear density fluctuations and the average cosmic mass density (e.g. Allen et al. 2011). Hence, observations on the abundance of galaxy clusters allow the establishment of the standard cosmological model (e.g. Vikhlinin et al. 2009; Rozo et al. 2010; Mantz et al. 2014; Planck Collaboration et al. 2016a; de Haan et al. 2016), but current cosmological constraints hinge on the accuracy in the estimation of mass.

The cross-correlation of galaxy clusters with the shapes of background galaxies, referred to as stacked lensing, is a unique means of measuring the average total matter distribution of the clusters in the foreground.

Stacked lensing analysis has the significant advantage of being independent from the dynamical state of a galaxy cluster, enabling the direct measurement of the gravitating mass of a cluster. It has been already applied to observational data sets and provided meaningful constraints on the relationship between multi-wavelength observables and the underlying cluster masses (e.g. Johnston et al. 2007; Umetsu et al. 2011; Okabe et al. 2013; Simet et al. 2017; Medezinski et al. 2018; Murata et al. 2018; Miyatake et al. 2019). In addition, large-scale amplitudes seen within the stacked lensing signal are expected to be associated with the clustering of dark matter halos of similar size (e.g. Covone et al. 2014). A combined analysis of the cluster abundance with the stacked lensing signal including the scales beyond a virial regime can be a powerful probe of the physics that lies beyond that of the standard model, such as massive neutrinos, the origin of the accelerating expansion of the universe, and the inflationary physics of the early universe (e.g. Oguri & Takada 2011; Shirasaki et al. 2016; Madhavacheril et al. 2017).

The mass density profile around a galaxy cluster is relevant to the stacked lensing analysis and accurate modeling of this profile is therefore essential for future cosmological analysis using galaxy clusters. It is commonly assumed that the density profile of a cluster solely depends on the mass at a given redshift, but this is not always valid. Numerical studies have suggested that the density profiles of dark matter halos can be expressed in a single universal form (e.g. Navarro et al. 1997), but the characteristic scales in the universal profiles will depend on the history of the mass accretion of the halos (e.g. Bullock et al. 2001; Wechsler et al. 2002; Ludlow et al. 2013). In addition, the large-scale amplitudes found within mass density profiles are usually parametrized with a linear bias parameter and the halo biases of clusters can depend not only on their masses, but also on other properties defined in their inner density profiles (e.g. Gao & White 2007; Faltenbacher & White 2010). On the scale of galaxy-clusters, the extent to which the mass assembly history can change the halo bias is still controversial. The latest cosmological simulations enable us to study the dependence of secondary parameters (other than mass) on the halo bias and it is apparent that the clustering of large halos is insensitive to the half-mass redshift (Mao et al. 2018), but a detailed characterization of the mass assembly history may be required to assess the assembly bias of cluster-sized halos (Chue et al. 2018).

As pointed out in the literature (e.g. Zemp 2014; Chue et al. 2018), one issue in studying mass assembly history is the definition of halo mass in numerical simulations. The spherical over-density (SO) mass has commonly been adopted in previous studies of mass assembly history, defined by

$$M_{\Delta}(z) = \frac{4}{3}\pi R_{\Delta}^3(z) \Delta(z) \rho_{\text{ref}}(z), \quad (1)$$

where $\Delta(z)$ is an SO parameter and $\rho_{\text{ref}}(z)$ is a reference density. Diemer et al. (2013) have derived that the time evolution of an SO mass can depend on the physical mass accretion outside the dark matter halos and on the evolution in the redshift of the reference density. Even if a dark matter halo has a completely static density profile with regards to its physical coordinates and there are no physical mass accretions, the SO mass can evolve over time. This evolution is referred to as the pseudo evolution. There have been numerous efforts to quantify and describe pseudo evolution using numerical simulations in the literature. Cuesta et al. (2008) introduced a new halo boundary defined by the innermost radius at which there is zero mean radial velocity and then studied the relationship between the new boundaries and the commonly adopted SO radii. Diemer et al.

(2013) have constructed a novel means of estimating the amount of pseudo evolution using the halo density profiles at two different redshifts. Zemp (2014) has investigated the pseudo evolution for various SO mass definitions by using an enclosed mass with a fixed physical scale. Wetzel & Nagai (2015) have explored the redshift evolution of the density profiles of dark matter and baryons in the context of pseudo evolution, whereas De Boni et al. (2016) have derived a relationship between the mass profile and mass accretion rate, and validated this relationship with numerical simulations.

It is important to study the amount of pseudo evolution that has occurred in the SO masses to refine our understanding of the mass assembly history of massive dark matter halos, and to develop a more accurate model of the stacked lensing signals from galaxy clusters. In particular, most previous studies have relied on numerical simulations with a small volume and/or a large time interval, leading to a situation where a detailed description of the pseudo evolution of individual cluster-sized halos is still unclear. In this study, we measure the amount of pseudo evolution that has taken place to the SO masses of cluster-sized halos by tracking the time evolution of their density profiles along with their merger histories in N -body simulations with a fine snapshot spacing. We also study the correlation among the pseudo evolution, the concentration of the inner density profile, age, and the density of the environment surrounding the halos. We then quantify the relationship between the amount of pseudo evolution and the averaged mass density profile, which is essential for the practical application of stacked lensing analysis for galaxy clusters.

The paper is organized as follows. In Section 2, an overview of the time evolution of the SO mass and introduce two common definitions for SO mass. In Section 3, we describe the N -body simulations and how to quantify the amount of pseudo evolution in the simulations. The results are presented in Section 4. Finally, the conclusions and discussions are provided in Section 5.

2. TIME EVOLUTION OF ENCLOSED MASS WITHIN A SPHERE

To study the mass distribution around galaxy clusters, a spherically symmetric mass density profile is considered $\rho(r, z)$, where r is the cluster-centric radius and z is the redshift under investigation. Using this spherical density profile, the SO mass can be defined (Eq. [1]) as

$$M_{\Delta}(z) = \int_0^{R_{\Delta}(z)} 4\pi r^2 dr \rho(r, z). \quad (2)$$

As introduced in Diemer et al. (2013), the redshift evolution of an SO mass M_{Δ} can be decomposed into

two terms:

$$\frac{dM_{\Delta}(z)}{dz} = 4\pi R_{\Delta}^2(z)\rho(R_{\Delta}, z)\frac{dR_{\Delta}(z)}{dz} + \int_0^{R_{\Delta}(z)} 4\pi r^2 dr \frac{d\rho(r, z)}{dz}, \quad (3)$$

where the first term in the right-hand side represents the pseudo evolution caused by the change in SO radius and the second term determines the evolution of the mass due to the actual growth of the density profile. The amount of pseudo evolution in the actual redshift evolution of an SO mass would be an important integrand in understanding the mass accretion history of a dark matter halo on a physical basis. Diemer et al. (2013) have studied the amount of pseudo evolution between $z = 0$ and 1 for a wide range of halo masses with N -body simulations. It would be worth noting that the results in Diemer et al. (2013) are still based on the density profiles of halos at $z = 0$ and their progenitors at $z = 1$. Although Diemer et al. (2013) included lower and upper limits, a direct estimate of the amount of pseudo evolution that has occurred on the scale of galaxy-cluster is yet to be obtained (but, see Diemand et al. 2007, for the direct estimate on galaxy scales). In this study, we measure the amount of pseudo evolution that has taken place in an SO mass between two redshifts by using ~ 30 snapshots of N -body simulations.

There are two conventional choices for the reference density in Eq. (1). One is the mean matter density which is denoted as $\bar{\rho}_m$ in this study, and another is the critical density of the universe denoted as ρ_c . Throughout this study, we use the definition of SO mass with respect to 200 times $\bar{\rho}_m$ as well as the virial SO mass which is represented by $\Delta_{\text{vir}}(z)$ times ρ_c , where Δ_{vir} is given by the spherical collapse model (Bryan & Norman 1998). For the former and the latter, we denote M_{200b} and M_{vir} , respectively.

3. METHOD

3.1. Simulation design

We run cosmological N -body simulations to study the time evolution of the density profiles around the galaxy clusters. We use the parallel Tree-Particle Mesh code GADGET2 (Springel 2005). With 1024^3 dark matter particles per unit volume of $500 h^{-1}$ Mpc on one side. We generate the initial conditions using a parallel code developed by Nishimichi et al. (2009) and Valageas & Nishimichi (2011), which employs the second-order Lagrangian perturbation theory (e.g. Crocce et al. 2006). The initial redshift is set to $z_{\text{init}} = 59$, where we compute the linear matter transfer function using CAMB (Lewis et al. 2000). We adopt the following parameters for

the simulations: present-day matter density parameter $\Omega_{m0} = 0.3156$, dark energy density $\Omega_{\Lambda} = 1 - \Omega_{m0} = 0.6844$, the density fluctuation amplitude $\sigma_8 = 0.831$, the parameter of the equation for the state of dark energy $w_0 = -1$, Hubble parameter $h = 0.6727$, and the scalar spectral index $n_s = 0.9645$. These parameters are consistent with the results from Planck 2015 (Planck Collaboration et al. 2016b). In our simulation, the particle mass is set at $1.020 \times 10^{10} h^{-1} M_{\odot}$, with a softening length of $20.4 h^{-1}$ kpc, which corresponds to 5 percent of the mean length of separation between particles. Note that the simulation setup is the same as that used for the fiducial high-resolution run in Nishimichi et al. (2018), except for the number of particles and the box length on one side. The impact from the difference in generating initial conditions and mass resolution on halo statistics has been studied in Nishimichi et al. (2018) in detail. Simulation parameters such as the time-integral accuracy have been calibrated to enable the resulting matter power spectrum to converge within a sub-percent level (Takahashi et al. 2012).

The primary purpose of this study is to reveal the extent to which pseudo evolution can account for the actual redshift evolution of an SO mass between a given range of redshifts. As shown in Eq. (3), we require a fine redshift resolution for the density profile $\rho(r, z)$ to accurately measure the pseudo evolution of an SO mass. To set the redshift interval between neighboring snapshots, we follow the method in Diemer (2017). We find the fiducial snapshot spacing in Diemer (2017) (i.e. the blue line in Figure 1 in Diemer (2017)), which can be approximated as

$$t_{\text{dyn}}(z)/\Delta t_{\text{snap}}(z) = 9.03 \times 10^{-4} [t_{\text{H}}(z)/\text{Gyr}]^3 + 1.4 \times 10^{-2} [t_{\text{H}}(z)/\text{Gyr}]^2 + 6.0 \times 10^{-2} [t_{\text{H}}(z)/\text{Gyr}] + 6.55, \quad (4)$$

where $t_{\text{H}}(z) = H^{-1}(z)$, Δt_{snap} is the snapshot spacing, and t_{dyn} is the dynamical time over which dark matter halos are present, which is defined by

$$t_{\text{dyn}}(z) = \frac{2R_{\Delta}}{v_{\Delta}} = 2^{3/2} H^{-1}(z) \left(\frac{\rho_{\Delta \text{ref}}(z)}{\rho_c(z)} \right)^{-1/2}, \quad (5)$$

where v_{Δ} represents the circular velocity at a radius of R_{Δ} . We use Eq. (4) to set the snapshot spacing within the unit for dynamical time with $\rho_{\Delta \text{ref}} = 200\bar{\rho}_m$. When setting the initial redshift to 20, we find that a total of 110 snapshots are available until $z = 0$. Our snapshot spacing roughly corresponds to 10% of the dynamical time in the redshift range of $0 < z < 1$. Note that the above method concerning the spacing of snapshots

has been calibrated to provide sufficient information to determine the location of the first apocenter of the N -body particles after the infall into a halo, or the splashback (see, [Diemer 2017](#), for details). Previous studies have shown that the splashback radius is in the range of 0.8 – 1.6 times R_{200b} , but this also depends on the mass accretion rate (e.g., [More et al. 2015](#)). This indicates that our snapshot spacing will be adequate to track the time evolution of the mass density distribution in the virial region for individual halos (but see [Appendix A](#) for possible systematic uncertainties on the estimate of pseudo evolution in this study).

3.2. Halo catalogs and merger tree

We use the phase-space halo finder ROCKSTAR ([Behroozi et al. 2013a](#)) to identify dark matter halos in the simulation and run the CONSISTENT-TREES code ([Behroozi et al. 2013b](#)) to generate the merger trees from the ROCKSTAR outputs. In the following analyses, we consider the time evolution of the density profiles of isolated halos at $z = 0$ with a peak height ν of greater than 1.5, except for the analysis in [Section 4.5¹](#). The peak height is commonly used to study the statistical properties of dark matter halos (e.g. [Press & Schechter 1974](#)) and is defined by $\nu = \delta_c / \sigma(M, z)$, where $\delta_c = 1.686$ is the critical overdensity in the spherical top hat collapse model ([Gunn & Gott 1972](#)), and $\sigma(M, z)$ is the variance of smoothed linear density fluctuations at a specific redshift z by a spherical top-hat filter. The top-hat radius R_{TH} in computing $\sigma(M, z)$ is set to $M_{200b} = 4\pi/3 \times \bar{\rho}_m(z=0)R_{TH}^3$. The use of M_{200b} to define the peak height is motivated by recent calibrations of halo statistics with a set of numerical simulations (e.g. [Tinker et al. 2008](#)) and the universality of outer density profiles ([Diemer & Kravtsov 2014](#)). In our adopted cosmological model, the peak height of $\nu = 1.5$ corresponds to $M_{200b} = 4.6 \times 10^{13} h^{-1} M_\odot$, which is resolved over 4600 particles in our simulation. For the progenitor of a distinct halo, we define the halo along its most massive progenitor branch at each redshift. We then construct the mass assembly history for each halo at $z = 0$ by using the virial mass M_{vir} of its progenitor.

3.3. Quantifying the amount of pseudo evolution

To study the pseudo evolution of an SO mass, we extract the spherically averaged density profiles $\rho(r)$ and the enclosed spherical mass $M(< r)$ of halos in 80 logarithmically spaced bins between $0.05R_{200b}$ and $10R_{200b}$. Note that we include all the particles around

halos within a sphere of $10R_{200b}$ when measuring $\rho(r)$ and $M(< r)$. For a given halo at $z = 0$, we then define the differences in the enclosed spherical masses of the progenitors within the neighboring redshifts of z_1 and $z_2 > z_1$ as

$$\Delta M_{\text{pseudo}}(z_1) \equiv M(< R_{\text{vir},1}, z_1) - M(< R_{\text{vir},2}, z_1), \quad (6)$$

where $M(< r, z)$ represents the enclosed spherical mass of the progenitor at redshift z within a sphere of r , and $R_{\text{vir},j}$ is the virial radius with respect to $\Delta_{\text{vir}}(z_j)$ times $\rho_c(z_j)$. [Eq. \(6\)](#) defines the redshift evolution of an SO mass between z_1 and z_2 , when the density profile is assumed to be static during the finite redshift range. It can be seen that [Eq. \(6\)](#) corresponds to the first right-hand side term in [Eq. \(3\)](#) when performing a Taylor expansion of $M(< R_{\text{vir},2}, z_1) \simeq M(< R_{\text{vir},1}, z_1) + 4\pi R_{\text{vir},1}^2 \times \rho(R_{\text{vir},1}, z_1)(R_{\text{vir},2} - R_{\text{vir},1})$. To find the virial radius R_{vir} from a binned enclosed mass profile, we use linear interpolation between two bins in logarithmic space. Finally, we estimate the cumulative amount of pseudo evolution in the SO mass between $z = 0$ and $z = 1$ as²

$$f_{\text{pseudo}}(0 < z < 1) \equiv \frac{\sum_{0 < z_1 < 1} \Delta M_{\text{pseudo}}(z_1)}{M_{\text{vir}}(z=0) - M_{\text{vir}}(z=1)}, \quad (7)$$

where $M_{\text{vir}}(z)$ contains unbounded particles in the above equation. It is worth noting that 29 snapshots are available between $z = 0$ and $z = 1$ in our simulations, leading to a typical redshift width between two neighboring snapshots of $\sim 0.03 - 0.04$.

Our estimation of [Eq. \(7\)](#) assumes no redshift evolution in the density profile between a small redshift interval. We evaluate possible systematic errors caused by the evolution between two snapshots in [Appendix A](#) and show that our estimates can have a 3–4% precision for the amount of pseudo evolution between $z = 0$ and $z = 1$.

Although we use the virial SO mass to study the amount of pseudo evolution throughout this study, it would be interesting to consider the amount of pseudo evolution using different definitions for mass. In [Appendix B](#), we examine the amount of pseudo evolution with an SO mass of M_{200b} . We find that the amount of pseudo evolution depends on the mass definition. To be specific, the width in the distribution of $f_{\text{pseudo}}(0 < z < 1)$ becomes narrower and the fraction of halos at $f_{\text{pseudo}} > 0.75$ is reduced if the halo mass is

¹ In [Section 4.5](#), we consider the amount of pseudo evolution for halos at the different redshifts of $z = 0.3, 0.6$ and 1 .

² Note that $f_{\text{pseudo}} = 1$ does not correspond to perfectly stable halo density profiles between a finite redshift interval in our definition. This is simply because of the existence of mass accretion onto halos at large radii beyond the SO radii of interest.

defined by M_{200b} . This is partly because the mass density profile within the radius of R_{200b} is more universal across different redshifts than the counterparts within the virial radius on average (Diemer & Kravtsov 2014). These results are in good agreement with the findings in Diemer et al. (2013).

3.4. Age and density environments of dark matter halos

Age is an important quantity to characterize the mass accretion history of a dark matter halo. To assess the correlation between age and the amount of pseudo evolution, we introduce two common indicators, halo concentration c_{vir} and the half-mass scale factor $a_{1/2}$. The former is defined by R_{vir}/r_s where r_s is the scale radius of a universal density profile as proposed in Navarro et al. (1997), while the latter is given by the scale factor $a = 1/(1+z)$ at which the mass of the progenitor is equal to half of its descendant halo mass at $z = 0$. Previous numerical studies have suggested that the halo concentration at a fixed redshift depends not only on the halo mass, but also on the mass assembly history (e.g. Bullock et al. 2001; Wechsler et al. 2002). In this study, we adopt the estimated value of r_s for individual halos by the ROCKSTAR and compute $a_{1/2}$ from the merger tree.

In addition to the age, the amount of pseudo evolution can depend on the environment surrounding a dark matter halo, because its exact value should closely relate to the mass accretion from outside the virial region (e.g. a slow accreting halo would have a more stable density profile, leading to a greater amount of pseudo evolution of the SO mass in a finite redshift range). The dynamics of mass accretion onto a dark matter halo will be regulated by the tidal tensor (e.g. Hahn et al. 2009),

$$T_{ij} \equiv \left[\frac{\partial^2}{\partial_i \partial_j} - \frac{1}{3} \delta_{ij}^{\text{K}} \nabla^2 \right] \phi, \quad (8)$$

where ϕ is the gravitational potential and δ_{ij}^{K} represents the Kronecker symbol. The tidal shear q^2 is a quantity that is promising for the characterization of the local environment of halos (Heavens & Peacock 1988; Catelan & Theuns 1996), which is commonly defined by

$$q^2 \equiv \frac{1}{2} \left[(\lambda_3 - \lambda_1)^2 + (\lambda_3 - \lambda_2)^2 + (\lambda_2 - \lambda_1)^2 \right], \quad (9)$$

where $\lambda_1 \leq \lambda_2 \leq \lambda_3$ are the eigenvalues of T_{ij} . The previous numerical studies have clearly demonstrated that tidal shear plays an important role in determining not only the dynamical properties, but also the large-scale clustering of halos (e.g. Wang et al. 2011; Baldauf et al. 2012; Shi et al. 2015; Paranjape et al. 2018). Motivated

by these results, we consider the tidal tensor induced by the mass density distribution surrounding a dark matter halo. To be specific, we compute an external tidal shear from the distribution of N -body particles as

$$T_{ij}^{\text{ext}} \equiv \sum_q \frac{Gm_p}{r_q^5} (3r_{q,i}r_{q,j} - \delta_{ij}^{\text{K}}r_q^2), \quad (10)$$

where m_p is the mass of a particle, \mathbf{r}_q is a vector locating the q -th particle from the center of a halo, and the summation runs over if r_q ranges between r_{min} and r_{max} . Throughout this study, we set $r_{\text{min}} = R_{200b}$ and $r_{\text{max}} = 10 R_{200b}$ when computing Eq. (10) for individual halos at $z = 0$. We then compute the tidal shear $(q^{\text{ext}})^2$ from the eigenvalues of T_{ij}^{ext} and cancel a trivial correlation between the tidal shear and the amplitude of over-density as follows:

$$\alpha = \frac{q^{\text{ext}}}{1 + \delta^{\text{ext}}}, \quad 1 + \delta^{\text{ext}} \equiv \frac{\int_{r_{\text{min}}}^{r_{\text{max}}} 4\pi r^2 dr \rho(r, z=0)}{4\pi/3 \bar{\rho}_{m0} (r_{\text{max}}^3 - r_{\text{min}}^3)} \quad (11)$$

where $\bar{\rho}_{m0} = \bar{\rho}_m(z=0)$. We denote the reduced tidal shear as α in this study. Note that Paranjape et al. (2018) introduced a similar quantity for tidal anisotropy defined from the smoothed density field around individual halos with a Gaussian smoothing scale of $4R_{200b}$ and showed that tidal anisotropy strongly correlates with halo bias. As shown in later parts of the paper, we also find a strong correlation between the reduced tidal shear α and the large-scale halo bias.

4. RESULTS

4.1. Visual impression

We first make a visual comparison between two dark matter halos with a virial mass of $M_{\text{vir}} = 10^{14} h^{-1} M_{\odot}$ at $z = 0$, but with a different amount of pseudo evolution in $M_{\text{vir}}(z)$ between $z = 0$ and 1. Figure 1 shows the mass accretion history of the two halos: the left represents the history of the halo with $f_{\text{pseudo}}(0 < z < 1) = 0.20$, while the right is for the halo with $f_{\text{pseudo}}(0 < z < 1) = 0.77$. For each, the small panel reveals the projected mass density with a projection depth of $2 h^{-1} \text{Mpc}$ at different redshifts. The halo and its progenitor are located at the center of each small panel. Note that the virial radius is found to be $1 h^{-1} \text{Mpc}$ at $z = 0$ in both panels.

The figure illustrates the rich large-scale structures that occur around a cluster-sized dark matter halo. Such structures may be associated with the mass accretion history. In the left, the halo has a small amount of pseudo evolution and this indicates that rapid growth has occurred in the mass density profile between $z = 0$ and 1. As shown in the figure, the clumpier and richer structures found beyond the virial regime are more

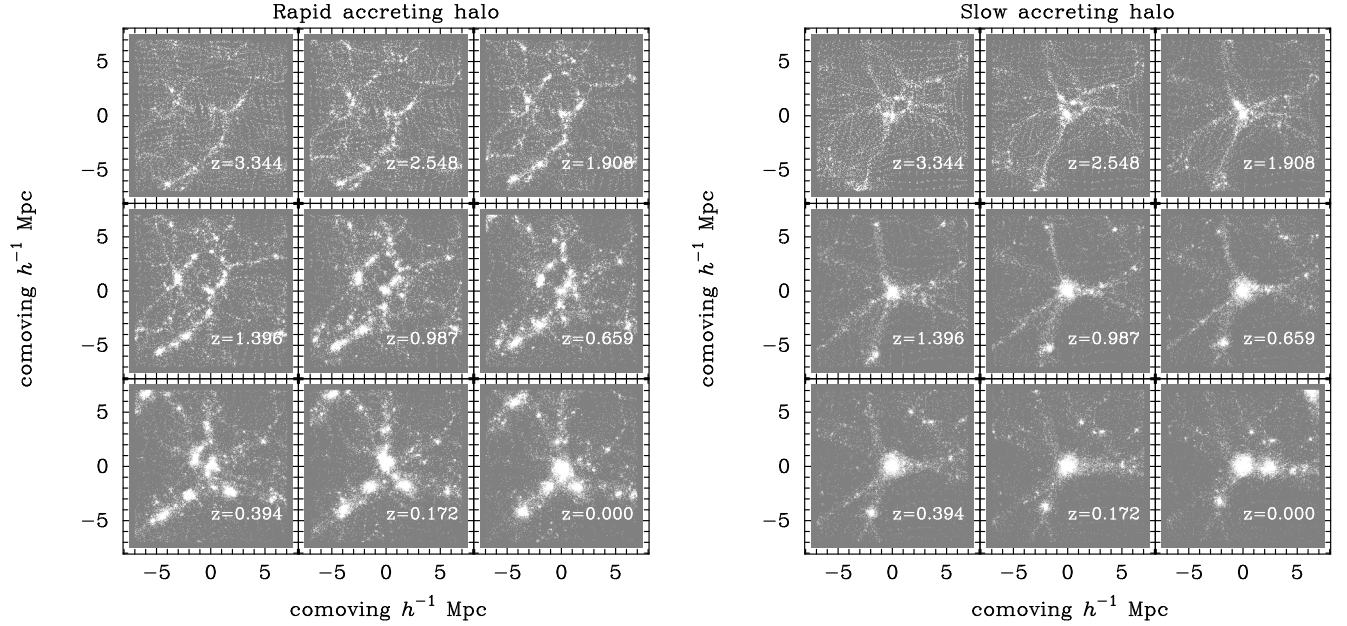


Figure 1. An example of mass accretion around galaxy clusters. In this figure, we consider two simulated clusters containing a mass of $10^{14} h^{-1} M_{\odot}$ within the virial radius. Note that the corresponding virial radius is approximately $1 h^{-1} \text{Mpc}$ at a redshift of $z = 0$. The left panels show the distribution of projected mass density around a cluster with a pseudo mass evolution fraction, from $z = 1$ to 0 , of $f_{\text{pseudo}}(0 < z < 1) = 0.20$ (i.e. 80% of the difference in virial mass between $z = 1$ and 0 can be accounted for by the physical mass accretion). The right panels represent a slowly accreting cluster with $f_{\text{pseudo}}(0 < z < 1) = 0.77$. The small panels in the left and right show the projected density at different redshifts from $z = 3.344$ to 0 . The cluster and its progenitor are located at the center of each image and the projection depth is set to be $2 h^{-1} \text{Mpc}$. See the definition of $f_{\text{pseudo}}(0 < z < 1)$ in Section 3.3.

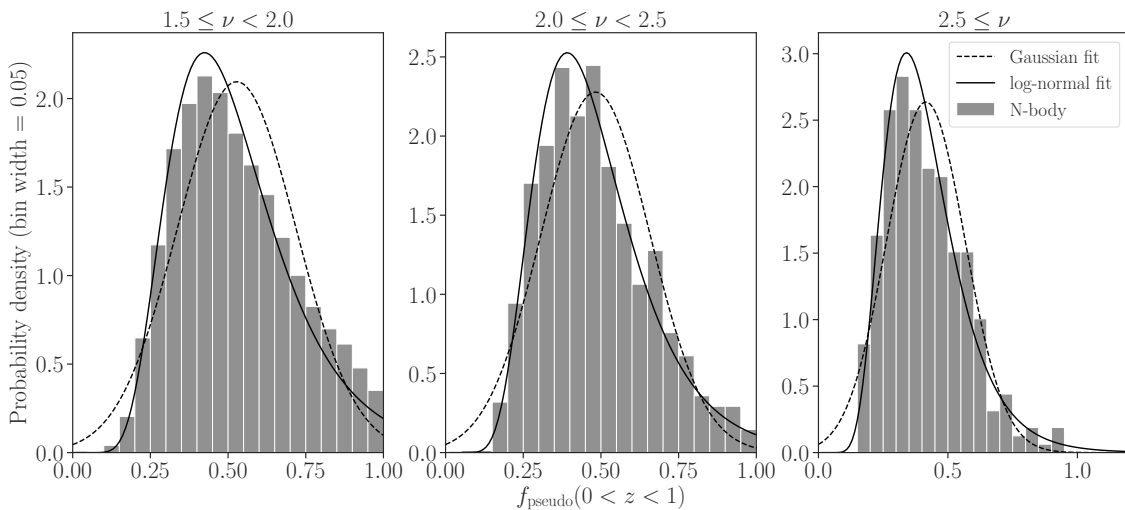


Figure 2. The probability distribution function (PDF) of the fraction of pseudo mass evolution from $z = 1$ to 0 , denoted as $f_{\text{pseudo}}(0 < z < 1)$. The left, middle, and right panels show the PDFs for clusters with different ranges in peak height $\nu = \delta_c/\sigma$, $1.5 \leq \nu < 2$, $2 \leq \nu < 2.5$, and $\nu \geq 2.5$, respectively. The gray histogram represents the result from the N -body simulations, while the dashed and solid lines show Gaussian and log-normal fits.

prevalent in the left as compared to the right. Those structures introduce an efficient mass accretion onto the

Table 1. Mean and root-mean square (RMS) of the amount of pseudo evolution of virial SO mass.

Range of ν	Mean (linear)	RMS (linear)	Mean (10-base log)	RMS (10-base log)
$1.5 \leq \nu < 2.0$	0.527	0.190	-0.307	0.167
$2.0 \leq \nu < 2.5$	0.482	0.175	-0.346	0.163
$\nu \geq 2.5$	0.415	0.151	-0.410	0.158

cluster-sized dark matter halo at the center of each small panel. Therefore, we expect the amount of pseudo evolution of an SO mass to be correlated with the environment of an individual halo (also, see De Boni et al. 2016, for the relation between the outer mass profile and the physical mass accretion).

4.2. Amount of pseudo mass evolution

We explore the statistical property of the amount of pseudo evolution $f_{\text{pseudo}}(0 < z < 1)$ as defined by Eq. (7). To study the halo mass dependence, we divide the halo sample into three sub-samples based on peak height $\nu = \delta_c/\sigma$. The bin of the peak height is set to $1.5 \leq \nu < 2$, $2 \leq \nu < 2.5$, and $\nu \geq 2.5$ at $z = 0$. After selection, we find the available number of halos are 10525, 1549, and 320 for the three ν bins, respectively. The mean halo masses at $z = 0$ in the three sub-samples are found to be $M_{200b} = 8.0 \times 10^{13} h^{-1} M_\odot$, $2.6 \times 10^{14} h^{-1} M_\odot$, and $7.1 \times 10^{14} h^{-1} M_\odot$. In the following, we limit the range of $f_{\text{pseudo}}(0 < z < 1)$ for individual halos to be between 0 and 1. The number of halos within our halo sample with $f_{\text{pseudo}} > 1$ is found to be 735, 45, and 1 for the samples with $1.5 \leq \nu < 2$, $2 \leq \nu < 2.5$, and $\nu \geq 2.5$, respectively. These minor populations are expected to have undergone tidal stripping, because $f_{\text{pseudo}} > 1$ indicates that the density profile around the virial radius decreases as $z = 1$. We also found a halo with $f_{\text{pseudo}} < 0$ in our sample and this ill-defined value is caused by the major merger at $z = 0.1$ and the significant change in its density profile after $z = 0.1$. Our estimation of the amount of pseudo evolution implicitly assumes that the density profile would evolve smoothly as a function of redshift. Therefore, we simply remove the halo with $f_{\text{pseudo}} < 0$ in this study. The measurements of f_{pseudo} for five halos were also not included because of a lack of information concerning the merger tree.

Figure 2 shows the histogram of $f_{\text{pseudo}}(0 < z < 1)$ for our three subsamples at $z = 0$. In each panel, the gray boxes represent the results of the simulation, while the solid and dashed lines are the Gaussian and log-normal fits, respectively. The fitting results are provided in Table 1. The relationship between averaged $f_{\text{pseudo}}(0 < z < 1)$ and halo mass is given by

$$\langle f_{\text{pseudo}}(0 < z < 1) \rangle = (-0.0193 \pm 0.0013) M_{200b,14}$$

$$+ (0.5421 \pm 0.0024), \quad (12)$$

where $M_{200b,14} = (M_{200b}/10^{14} h^{-1} M_\odot)$, and we find a clear decreasing trend in f_{pseudo} as a function of halo mass. The variance around Eq. (12) is approximated as $(-0.0022 \pm 0.0003) M_{200b,14} + (0.0379 \pm 0.0006)$, suggesting that more massive galaxy clusters have smaller scatters in f_{pseudo} .

Next, we study the correlation between the amount of pseudo evolution and other halo properties. Figure 3 summarizes the correlations measured in our simulation. In the figure, we consider three halo properties apart from the amount of pseudo evolution; the halo concentration c_{vir} , the half-mass time $a_{1/2}$, and the reduced tidal shear defined in Eq. (11). In each panel of Figure 3, the thick and dashed contour lines show the correlations for halos with $1.5 \leq \nu < 2$ and $2 \leq \nu < 2.5$, while the red points illustrate halos with $\nu \geq 2.5$. We find that the amount of pseudo evolution shows a positive correlation with c_{vir} , while it is anti-correlated with the density of the environment beyond the virial scales α , and the halo age $a_{1/2}$. The positive correlation between f_{pseudo} and c_{vir} is expected because older halos are expected to include more stable density profiles, i.e. larger f_{pseudo} , with greater concentration (e.g. Bullock et al. 2001; Wechsler et al. 2002). Conversely, a weak anti-correlation between f_{pseudo} and a reduced tidal shear α may be understood via the following. A density environment with larger α indicates the presence of richer filamentary structures around a halo. Such filaments can induce an efficient mass accretion onto the halo from the scales beyond the virial regime, implying that physical mass accretion can be a main driver in the time evolution of virial SO mass, i.e. smaller f_{pseudo} . This argument is supported by the visual comparison shown in Figure 1. It is also worth noting that our estimation of tidal shear is mainly determined from the density structures around the virial radius (see Eq. [10]). In fact, we found no correlations of f_{pseudo} between the tidal tensors of a smoothed density field with a Gaussian smoothing scale of $10 h^{-1} \text{Mpc}^3$. Hence, we expect the amount of pseudo

³ To be specific, we use the quantity α_R defined in Eq. (10) in Paranjape et al. (2018) for an indicator of tildes. The correlation of f_{pseudo} with α_R is found to be less than 0.10 for $\nu \geq 1.5$ when adopting a smoothing scale of $10 h^{-1} \text{Mpc}$.

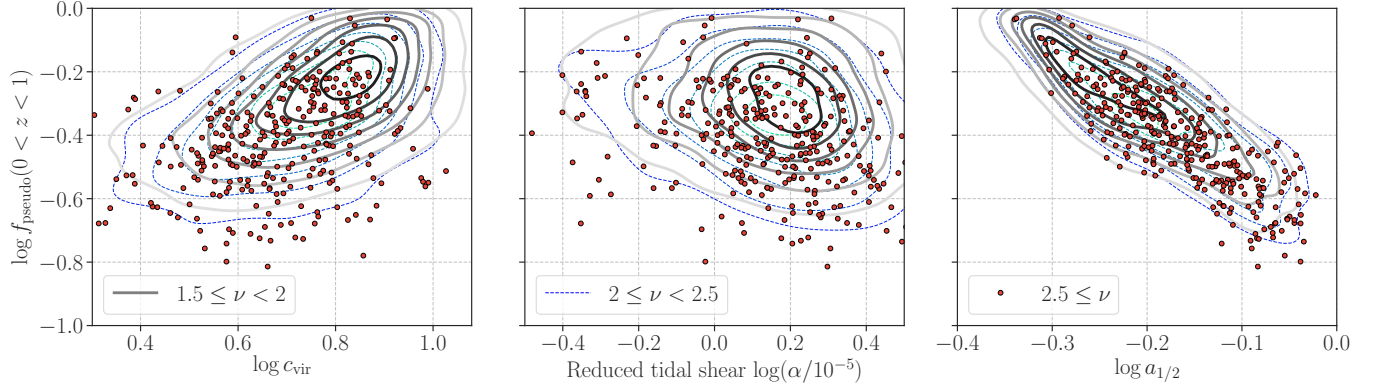


Figure 3. Scatter plot between the fraction of pseudo mass evolution from $z = 1$ to 0 ($f_{\text{pseudo}}(0 < z < 1)$) and other halo properties. The left, middle, and right panels show the correlation between $f_{\text{pseudo}}(0 < z < 1)$ and concentration, reduced tidal shear α and half-mass scale factor $a_{1/2}$, respectively. In each panel, the solid contours represent the results for the clusters in the peak height range $1.5 < \nu < 2$, the dashed contours represent clusters with $2 < \nu < 2.5$, and the red points are clusters with $\nu > 2.5$.

Table 2. Correlation of the amount of pseudo evolution of virial SO mass with other halo properties. We denote the halo concentration, the half-mass scale factor, and the reduced tidal shear as c_{vir} , $a_{1/2}$ and α , respectively. See Eq. (11) for our definition of α . Note that \log represents a 10-base logarithm.

Range of ν	$\log c_{\text{vir}} - \log f_{\text{pseudo}}$	$\log(\alpha/10^{-5}) - \log f_{\text{pseudo}}$	$\log a_{1/2} - \log f_{\text{pseudo}}$
$1.5 \leq \nu < 2.0$	0.319	-0.336	-0.828
$2.0 \leq \nu < 2.5$	0.429	-0.253	-0.810
$\nu \geq 2.5$	0.400	-0.142	-0.760

evolution to depend on the density environment close to the virial radius, but not on the large-scale environment. The cross correlation coefficients in logarithmic space are summarized in Table 2.

4.3. Stacked density profile

We then study the connection between the pseudo evolution in cluster SO masses to and spherical density profiles and the amplitude of large-scale clustering. For this purpose, we perform a stacking analysis of spherical density profiles for a set of halos. We here focus on halos with $\nu \geq 2$ at $z = 0$. Note that the average halo mass is found to be $3.3 \times 10^{14} h^{-1} M_{\odot}$, which is a typical mass of a galaxy cluster at low redshift. Each halo has the scale radius r_s , the reduced tidal shear α , and the amount of pseudo evolution in its virial SO mass of between $z = 0$ and 1, $f_{\text{pseudo}}(0 < z < 1)$. We divide the parent halo sample into three by using a secondary parameter ($c_{200b} = R_{200b}/r_s$, α , and f_{pseudo}) so that the average halo mass and the number of each subsamples will be equal. After dividing the halo sample, we find that the average masses of the halos within the three subsamples match within the level of a few percent. We then stack the density profile for the parent samples and

the subsamples with 33% lower and higher values of a secondary parameter.

Figure 4 shows the results of the stacking analysis of the spherical density profiles. From left to right, we consider the subsamples defined by c_{200b} , f_{pseudo} , and α . In each top panel, the black solid line shows the stacked profile of the parent halo sample, while the blue dashed and red dotted-dashed lines are for the lower and higher subsamples. In each bottom panel, we show the fractional difference in the stacked profiles between the higher and lower subsamples. Note that the top panels of Figure 4 are given in the form $\sim r^2 \rho(r)$ to allow the easy location of the scale radius of the stacked density profiles where $d \ln \rho(r)/d \ln r = -2$.

First we confirm that the stacked density profile of those halos with lower concentrations shows a larger amplitude outside of the virial radius compared to the full sample, as in previous studies (e.g. Wechsler et al. 2006). Since the amplitude of a stacked density profile outside a virial regime is closely associated with the linear halo bias (e.g. Hayashi & White 2008), the top left panel in Figure 4 represents the subsample with a lower c_{200b} , which has the larger linear halo bias and is consistent with the known secondary halo bias on galaxy-

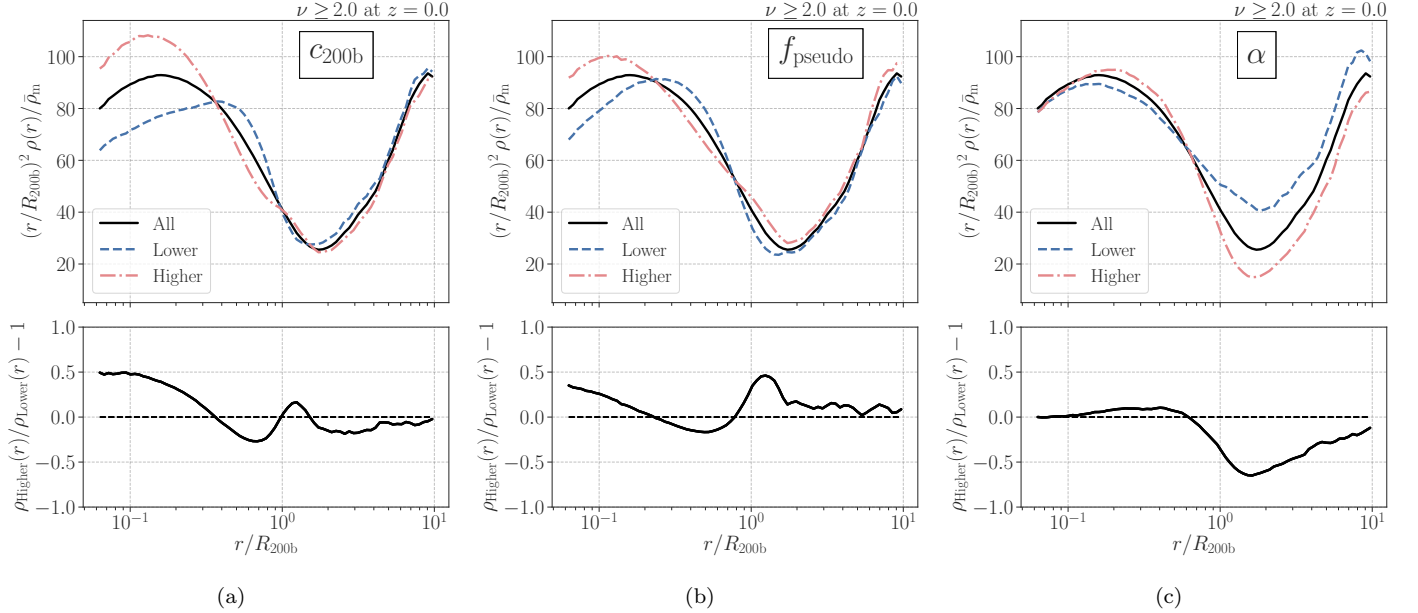


Figure 4. Stacked mass density profile of cluster-sized dark matter halos with a peak height parameter larger than 2. In each top panel, the solid line shows the result for a full sample, while the dashed and dotted-dashed lines show the stacked profiles for subsamples with 33% lower and higher values of a secondary halo parameter, respectively. In the bottom panels, we show the fractional difference in the stacked density profiles between two subsamples. In this figure, we consider three secondary parameters: (a) halo concentration c_{200b} , (b) the fraction of pseudo mass evolution from $z = 1$ to 0 and (c) reduced tidal shear α . Note that the tidal shear is computed from N -body particles in a spherical shell with an inner radius of R_{200b} and an outer radius of $10 R_{200b}$, where R_{200b} is the spherical over-density radius of each halo of 200 times the mean matter density.

cluster scales (e.g. Dalal et al. 2008). For subsamples with f_{pseudo} , the relationship between halo concentration and linear bias is found to be inverted. The top middle panel in Figure 4 shows that the lower- f_{pseudo} subsample can have a lower concentration *and* a lower linear bias. As shown in Figure 3, the amount of pseudo evolution f_{pseudo} is correlated with the halo concentration. Therefore, it is a natural consequence that a stacked density profile of halos with lower f_{pseudo} will have a lower c_{200b} . Note that our stacked analysis of density profiles split by halo property is found to be consistent with the results in Diemer & Kravtsov (2014). We confirmed that halos with high mass accretion rates exhibit very different median profiles compared to their slowly accreting counterparts, while lower-concentration samples have steeper outer density profiles.

To understand why the lower- f_{pseudo} subsample can have the smaller linear bias, we look into the stacked density profile of the subsamples with the reduced tidal shear α . The top right panel in Figure 4 presents the stacked density profiles for the subsamples divided by α . It clearly shows that the reduced tidal shear α has only a limited effect on the inner density profile, i.e. the halo concentration. On the other hand, the value of α is tightly anti-correlated with the linear halo bias. Hence, Figure 4 highlights that the inner stacked density profile

for halos with different f_{pseudo} provides the correlation between f_{pseudo} and c_{200b} (or halo age), whereas the outer profile is probably governed by the anisotropy in the density of the environment.

4.4. Linear bias and concentration

To quantify the results in Section 4.3, we infer the linear bias and the halo concentration from statistical analyses of the halo samples.

We evaluate the linear halo bias by using an auto power spectrum of the matter density field $P_{\text{mm}}(k)$, and a cross power spectrum between matter and the halo overdensity fields $P_{\text{hm}}(k)$. To measure these power spectra, we construct matter and halo overdensity fields from N -body particles and halos using Clouds-in-Cell (CIC) assignment, respectively. For the CIC assignment, a 1024^3 cubic lattice is adopted. The power spectrum is computed in Fourier space with linear spaced bins and a bin size of $\Delta k = 0.012 h \text{ Mpc}^{-1}$. We then estimate the linear halo bias b_L so as to minimize the following χ^2 statistic:

$$\chi^2(b_L) = \sum_{k_i \leq k_{\text{max}}} \frac{[P_{\text{hm}}(k_i) - b_L P_{\text{mm}}(k_i)]^2}{\sigma_{P_{\text{hm}}}^2(k_i)}, \quad (13)$$

where we set $k_{\text{max}} = 0.1 h \text{ Mpc}^{-1}$ and $\sigma_{P_{\text{hm}}}$ is the Gaussian error of the cross power spectrum P_{hm} . The Gaus-

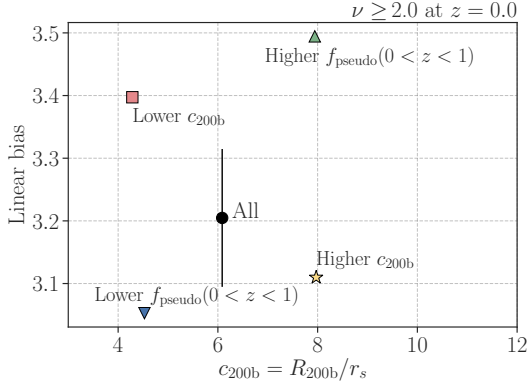


Figure 5. The relationship between linear bias and concentration for present-day clusters with a peak height larger than 2. The black point shows the results for the full sample and the error bar is the Gaussian error of the estimation of the linear bias in the simulation. The different symbols represent the bias-concentration relationships of the subsample divided by the secondary parameters of concentration (c_{200b}) or the amount of pseudo mass evolution, $f_{\text{pseudo}}(0 < z < 1)$.

sian error of P_{hm} is evaluated as

$$\sigma_{P_{\text{hm}}}^2(k_i) = \frac{P_{\text{hh}}(k_i)P_{\text{mm}}(k_i) + P_{\text{hm}}^2(k_i)}{N_{\text{mode}}(k_i)}, \quad (14)$$

where $N_{\text{mode}}(k_i)$ is the number of Fourier modes in i -th bin, and P_{hh} is the auto power spectrum of the halo overdensity field including the shot noise. We also estimate the uncertainty in b_L by imposing $\chi^2 - \chi_{\text{min}}^2 \leq 1$, where χ_{min}^2 is the minimum χ^2 statistic.

We also re-measure the halo concentration from the stacked density profile in a radius range of $0.05 \leq r/R_{200b} \leq 0.5$ by using the profile proposed in Navarro et al. (1997)⁴,

$$\rho_{\text{NFW}}(x) = \frac{\rho_s}{(c_{200b}x)(1 + c_{200b}x)^2}, \quad (15)$$

where $x = r/R_{200b}$ and $c_{200b} = R_{200b}/r_s$. the fit was carried out using the non-linear least-squares Levenberg-Marquardt algorithm (Press et al. 1992) by minimizing the χ^2 -fitting metric defined as

$$\chi_\rho^2 = \sum_{i=1}^{N_{\text{bin}}} [\ln \rho(x_i) - \ln \rho_{\text{NFW}}(x_i | \rho_s, c_{200b})]^2, \quad (16)$$

⁴ This re-fitting is needed because the concentration of a stacked profile is not generally the mean or median of the concentrations of the individual profiles.

where N_{bin} is the number of radial bins in the stacked density profile. We find that $N_{\text{bin}} = 32$ when limiting the radial range to be $0.05 \leq r/R_{200b} \leq 0.5$.

Figure 5 summarizes the fitting results of the linear halo bias b_L and the concentration c_{200b} for different halo samples. The figure shows that the amount of pseudo evolution f_{pseudo} can change the linear halo bias by 6.25%. This difference in the linear bias with respect to f_{pseudo} is at a similar level to the known secondary bias due to the halo concentration.

4.5. Varying halo masses and redshifts

So far, we have focused on halos at $z = 0$ and the amount of pseudo evolution that has taken place in the virial SO mass since $z = 1$. In this section, we generalize the aforementioned results by considering the different redshift ranges. We therefore consider three halo samples at different redshifts $z = 0.3, 0.6$, and 1 , and estimate the amount of pseudo evolution since $z = 1.6, 2$, and 3 as in Section 3.3, respectively. We denote the amount of pseudo evolution from $z = z_i$ to z_f as $f_{\text{pseudo}}(z_f < z < z_i)$. For a given z_f , we determine the initial redshift z_i by imposing $t(z_i) = t(z_f) - 2t_{\text{dyn}}(z_f)$, where $t(z)$ represents the cosmic time at redshift z and $t_{\text{dyn}}(z)$ is the dynamical time for the SO mass with respect to 200 times $\bar{\rho}_m$. In our adopted cosmological model, this criteria sets $z_i = 1, 1.6, 2$ and 3 for $z_f = 0, 0.3, 0.6$, and 2 , respectively. We then perform the stacking analysis of the spherical density profiles for halo catalogs at $z = 0.3, 0.6$, and 1 with the amount of pseudo evolution used for the selection. We select the halo samples with 33% higher and lower f_{pseudo} at different redshifts as in Section 4.3.

Figure 6 summarizes the correlation between f_{pseudo} and the stacked density profiles at different redshifts when the minimum halo mass for each redshift is set at $\nu \geq 2$. We find the amount of pseudo evolution and the stacked density profiles are correlated with each other in a similar manner even if the halo samples at $z > 0$ are taken into consideration. We also confirm that the trend observed in Figure 6 still remains if we vary the range in the peak height to be $\nu \geq 1.5$ or ≥ 2.5 . Therefore, the relationship between the stacked density profile of the cluster-sized halos and the amount of pseudo evolution is nearly universal across all masses and redshifts as long as the halos are selected with respect to the peak height ν .

In Appendix C, we extensively study the correlation between the amount of pseudo evolution, the linear bias, and the halo concentration at different redshifts and masses. We find a similar trend to that shown in Figure 5 for various redshift and mass bins.

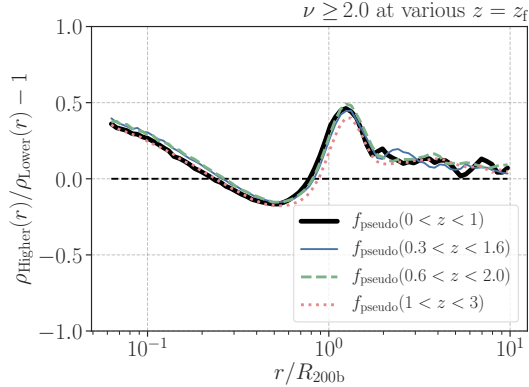


Figure 6. Similar to the bottom middle panel of Figure 4, but we here include the results at different redshifts. In this figure, we consider the halo sample with $\delta_c/\sigma(M_{200b}, z) \geq 2$ at $z = 0, 0.3, 0.6,$ and 1 . For a given sample at $z = z_f$, we measure the stacked density profiles of the halo sample with different selections for the amount of pseudo evolution since $z = z_i$, denoted as $f_{\text{pseudo}}(z_f < z < z_i)$. The different lines in the figure show the fractional difference in the stacked density profiles between two subsamples with 33% higher and lower $f_{\text{pseudo}}(z_f < z < z_i)$ at various z_f .

5. DISCUSSION AND CONCLUSION

In this study, we studied the mass accretion around the virial region of a sample of galaxy clusters with N -body simulations in detail. Using a time series of the N -body simulation, we measured the redshift evolution of the spherical over-density (SO) mass of a galaxy cluster, along its mass accretion history. Moreover, we evaluated the evolution of SO masses due to the change in a reference density, i.e. the pseudo evolution, on an individual basis at a galaxy-cluster scale. The amount of pseudo evolution is expected to be important for a complete understanding of the mass evolution around galaxy clusters over a cosmic age. Our findings are summarized as follows:

- (i) For clusters with virial masses of $10^{14} h^{-1} M_\odot$ at $z = 0$, $52 \pm 19\%$ the difference in the SO mass between $z = 0$ and 1 is accounted for by the pseudo evolution. The amount of pseudo evolution in a virial SO mass between $z = 0$ and 1 , denoted as $f_{\text{pseudo}}(0 < z < 1)$, generally decreases as M_{200b} increases, where M_{200b} is the SO mass with respect to 200 times the mean matter density at $z = 0$. The variance around the mean relationship between $f_{\text{pseudo}}(0 < z < 1)$ and M_{200b} is also found to decrease in more massive halos.

- (ii) The amount of pseudo evolution between $z = 0$ and 1 can be correlated with a common estimation of halo age, the half-mass scale factor $a_{1/2}$, and the concentration of the inner density profile. In addition, we found a correlation between $f_{\text{pseudo}}(0 < z < 1)$ and the tidal shear in the outskirts of galaxy clusters. Our numerical simulation shows that halos with higher $f_{\text{pseudo}}(0 < z < 1)$ tend to be older, more concentrated, and reside in environments with poorly developed filamentary structures.
- (iii) The stacked density profile of a sample of galaxy clusters depends on the amount of pseudo evolution between $z = 0$ and 1 . The profile inside a virial radius of $z = 0$ is more concentrated if one preferentially chooses galaxy clusters with higher $f_{\text{pseudo}}(0 < z < 1)$. Interestingly, we found that subsamples with higher $f_{\text{pseudo}}(0 < z < 1)$ can show a larger amplitude in the stacked density profile beyond the virial radius. This trend is a counter-example of the known secondary bias by halo concentration (e.g. Wechsler et al. 2006) and is caused by the correlation between $f_{\text{pseudo}}(0 < z < 1)$ and the tidal shear around clusters. We estimated that the linear halo bias can be changed at the $\sim 6.25\%$ level due to the amount of pseudo evolution that has occurred in galaxy clusters with $M_{200b} = 3.3 \times 10^{14} h^{-1} M_\odot$ at $z = 0$.
- (iv) We showed that the stacked density profile of galaxy clusters at $z > 0$ is also correlated with the amount of pseudo evolution within a finite redshift range. For galaxy clusters at the four different redshifts $z = 0, 0.3, 0.6$ and 1 , the impact of the amount of pseudo evolution on the stacked density profiles is found to be similar if the clusters are selected based on the peak height parameter $\nu = \delta_c/\sigma(M_{200b}, z)$, where $\delta_c = 1.686$ and σ is the top-hat mass variance at redshift z . We also found the secondary bias due to the amount of pseudo evolution is more prominent in lower- ν halos than higher- ν halos.

Although our results concerning the amount of pseudo evolution are not expected to be significantly affected by complex baryonic feedback processes, the halo concentration of galaxy clusters would depend on the detailed astrophysics (e.g. Duffy et al. 2010; Fedeli 2012; Schaller et al. 2015; Shirasaki et al. 2018). In addition, it is still uncertain if baryons experience pseudo-evolution after accretion onto cluster-sized halos (but see Wetzel & Nagai 2015, for the recent study). Therefore, more

thorough study with hydrodynamical simulations is required for the accurate modeling of halo concentration as a function of f_{pseudo} .

Furthermore, the selection function of galaxy clusters at multiple wavelengths could be related to the amount of pseudo evolution of the SO masses. At least, the selection of galaxy clusters by weak lensing analysis will be subject to the amount of pseudo evolution, because the selection is based on the projected mass density around individual clusters (e.g. Hamana et al. 2004, 2012; Shirasaki et al. 2015; Miyazaki et al. 2018). We expect that clusters selected by lensing may preferentially have higher amounts of pseudo evolution, because such clusters can have larger linear bias and concentration, and therefore the associated lensing signal of such structures can be boosted. It would also be worth exploring whether the amount of pseudo evolution can be correlated with any other halo properties such as shape, the

presence of substructures, spin, and anisotropy of the velocity. These possible correlations would be important to understand the secondary bias on the scale of galaxy clusters (e.g. Gao & White 2007; Faltenbacher & White 2010; Mao et al. 2018) and we leave these questions for future study.

The author thanks the anonymous referee for reading the paper carefully and providing thoughtful comments, many of which have resulted in changes to the revised version of the manuscript. This work is in part supported by MEXT KAKENHI Grant Number (18H04358, 19K14767). Numerical computations were in part carried out on Cray XC50 at Center for Computational Astrophysics, National Astronomical Observatory of Japan.

APPENDIX

A. SYSTEMATIC UNCERTAINTIES IN THE ESTIMATE OF AMOUNTS OF PSEUDO EVOLUTION

We here summarize the investigation of possible systematic effects on measuring the amount of pseudo evolution using a time series of N -body simulations.

As in Section 3.3, we estimate the amount of pseudo evolution of the virial SO mass assuming that the mass density profiles can be almost static between two snapshots in our simulations. Under this static-profile approximation, we can write the pseudo-evolved masses from $z = z_1$ to $z_2 > z_1$ as Eq. (6). Similarly, we can estimate the pseudo-evolved masses in descending order of redshift as

$$\Delta M'_{\text{pseudo}}(z_2) \equiv M(< R_{\text{vir},1}, z_2) - M(< R_{\text{vir},2}, z_2), \quad (\text{A1})$$

As discussed in Diemer et al. (2013), assuming the mass density profiles evolve monotonically at all radii between two redshifts, Eqs. (6) and (A1) can provide the upper and lower limits of the pseudo-evolved masses, respectively. Hence, we introduce the following quantity to assess the systematic error in the estimate of f_{pseudo} ,

$$\Delta f_{\text{pseudo}}(0 < z < z_i) \equiv 1 - \frac{\sum_{0 < z < z_i} M'_{\text{pseudo}}(z)}{\sum_{0 < z < z_i} M_{\text{pseudo}}(z)}. \quad (\text{A2})$$

The left panel of Figure 7 shows $\Delta f_{\text{pseudo}}(0 < z < z_i)$ as a function of the initial redshift z_i and the virial SO mass at $z = 0$. We find that the time evolution in the mass density profiles between two snapshots can a 3 – 4% effect our estimates of f_{pseudo} at $z_i = 1$.

Apart from the time evolution, we also study the impact of the outer mass profiles on the estimate of f_{pseudo} . For this purpose, we use another estimation of the pseudo-evolved masses based on the Navarro-Frenk-White (NFW) profiles (Eq. [15]) for individual halos,

$$\Delta M_{\text{pseudo,NFW}}(z_1) \equiv M_{\text{NFW}}(< R_{\text{vir},1}, z_1) - M_{\text{NFW}}(< R_{\text{vir},2}, z_1), \quad (\text{A3})$$

where $M_{\text{NFW}}(< R, z)$ represents the enclosed mass profile given by the NFW profile. To compute Eq. (A3), we use the scale radii (r_s) and the virial SO masses (M_{vir}) obtained from the ROCKSTAR algorithm on a halo-by-halo basis. In the right panel of Figure 7, the color map and the solid contours represent our fiducial estimate of f_{pseudo} (Eq. [7]) as a function of z_i and the present-day virial SO mass, while the red dashed contours are the counterparts based on Eq. (A3). The NFW-profile-based estimates are broadly consistent with the results in More et al. (2015). We found that the outer mass profile directly extracted from the simulations can affect the estimate of f_{pseudo} at $z_i = 1$ by $\sim 10\%$.

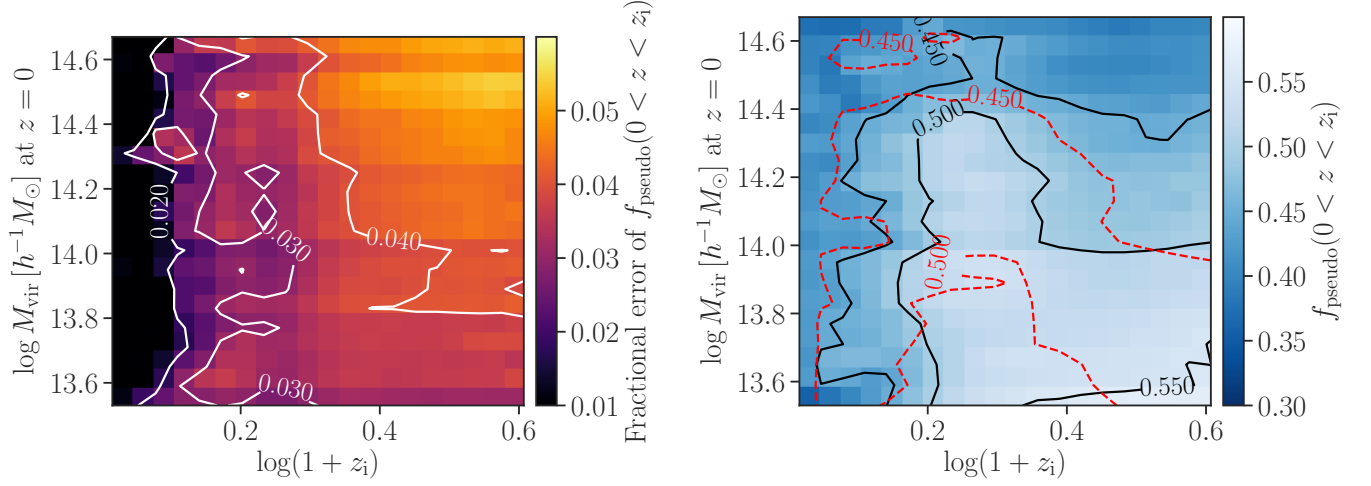


Figure 7. Systematic errors on the estimation of the amount of pseudo evolution f_{pseudo} . The left panel summarizes the systematic effect arising from the time evolution of the mass density profiles between two snapshots in our numerical simulations, while the right represents the impact of the contributions from the outer mass profile beyond the virial radius on the estimate of f_{pseudo} . In the left, we show the fractional difference between the lower and upper limits of f_{pseudo} , assuming that the density profiles grow monotonically at all radii. In the right panel, the colored map and the solid contours show f_{pseudo} as a function of the initial redshift z_i and the virial SO mass at $z = 0$, while the red dashed contours represent the estimates when we use the NFW profiles for individually simulated halos.

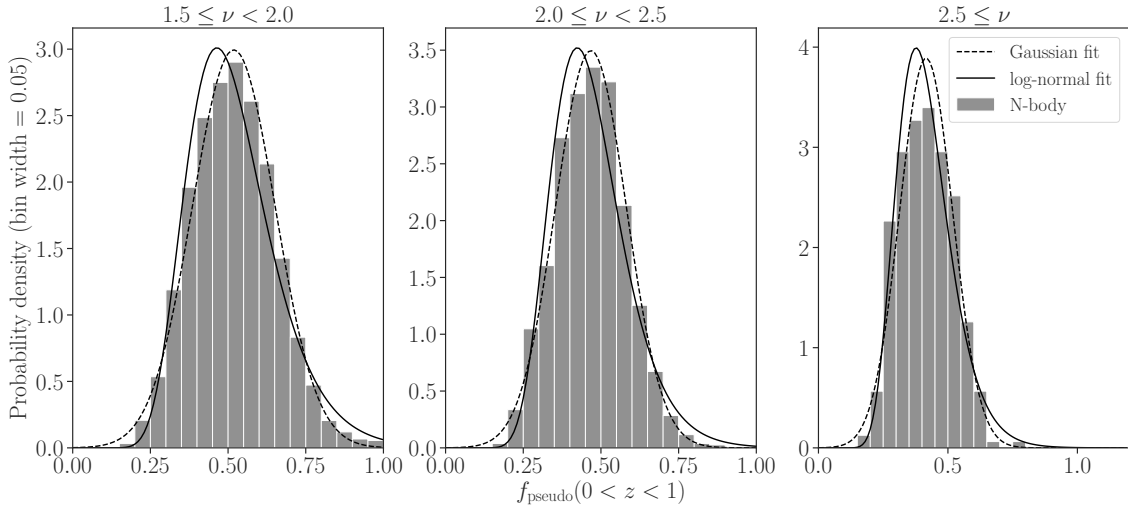


Figure 8. Similar to Figure 2, but we define the fraction of pseudo mass evolution by using the SO mass with respect to 200 times mean mass density.

B. THE PSEUDO EVOLUTION OF SO MASS WITH RESPECT TO 200 TIMES MEAN DENSITY

In this Appendix, we examine the amount of pseudo evolution of the SO mass with respect to 200 times mean matter density M_{200b} . We adopt a similar estimation to that used in Eq. (7), but replace the virial masses and radii with M_{200b} and R_{200b} , respectively. As in the main text, we consider halo samples with three different bins of peak height ν , $1.5 \leq \nu < 2$, $2 \leq \nu < 2.5$, and $2.5 \leq \nu$.

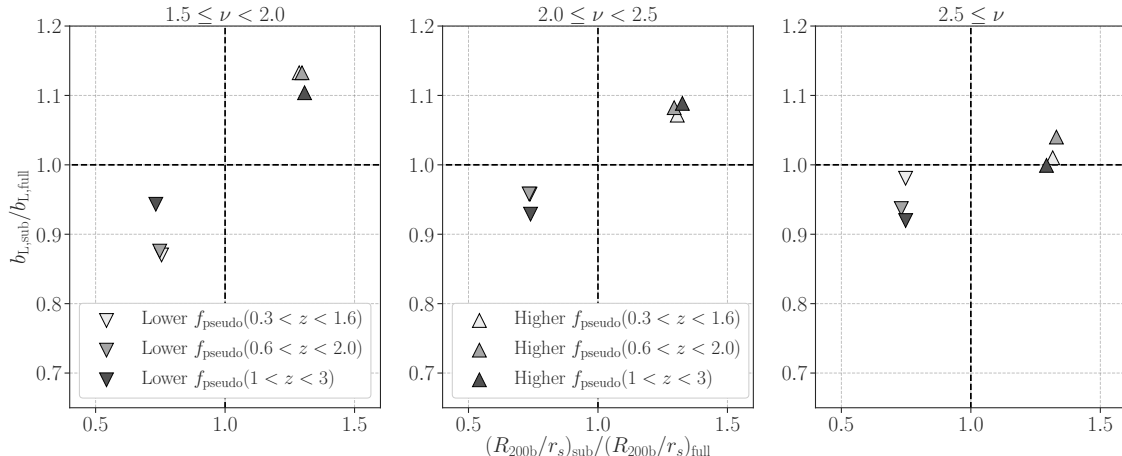


Figure 9. Similar to Figure 5, but here we show the results at different redshifts and halo masses. In this figure, we consider three different ranges of peak height $\nu = \delta_c/\sigma(M_{200b}, z)$. From left to right, the corresponding ν range is given by $1.5 \leq \nu < 2$, $2 \leq \nu < 2.5$ and $\nu \geq 2.5$, respectively. For a given ν range at $z = z_f$, we divide the halo sample by the amount of pseudo evolution between $z = z_f$ and z_i (denoted as $f_{\text{pseudo}}(z_f < z < z_i)$) and derive the linear halo bias b_L and the halo concentration R_{200b}/r_s . Each panel summarizes the fitted result of b_L and R_{200b}/r_s for the subsample with 33% higher and lower f_{pseudo} . Note that the bias and the halo concentration in this figure are normalized by the counterparts for the full sample.

Figure 8 shows the histogram of $f_{\text{pseudo}}(0 < z < 1)$ when using the SO mass of M_{200b} for our three subsamples at $z = 0$. In each panel, the gray boxes represent the simulation results, while the solid and dashed lines are the Gaussian fit and log-normal fits, respectively. Notably, the distribution of $f_{\text{pseudo}}(0 < z < 1)$ becomes narrower when the SO mass definition of M_{200b} is used than for the M_{vir} -counterparts, leading to simple Gaussian fits that can explain the simulation results. We find the relationship between the averaged $f_{\text{pseudo}}(0 < z < 1)$ for M_{200b} can be approximated by

$$\langle f_{\text{pseudo}}(0 < z < 1) \rangle = (-0.0186 \pm 0.0009)M_{200b,14} + (0.5311 \pm 0.0016), \quad (\text{B4})$$

where $M_{200b,14} = (M_{200b}/10^{14} h^{-1} M_{\odot})$. In addition, the variance around Eq. (B4) is given by $(-0.0014 \pm 0.0001)M_{200b,14} + (0.0185 \pm 0.0003)$.

C. THE CONNECTION OF THE AMOUNT OF PSEUDO EVOLUTION TO THE LINEAR BIAS AND THE CONCENTRATION AT VARIOUS REDSHIFTS

Figure 9 shows the impact of the amount of pseudo evolution on the linear halo bias b_L and the concentration R_{200b}/r_s at different redshifts and masses. We consider three bins of peak height parameter $\nu = \delta_c/\sigma(M_{200b}, z)$ at $z = 0.3, 0.6, \text{ and } 1$. In Figure 9, we set the range of ν to be $1.5 \leq \nu < 2$, $2 \leq \nu < 2.5$, and $\nu \geq 2.5$ from left to right. For a given range of ν at redshift z_f , we divide the halo sample into three by the amount of pseudo evolution as $z = z_i$. The redshift z_i is set to ensure the cosmic time interval between z_i and z_f is equal to double that of the dynamical time at redshift z_f . We then measure the linear halo bias b_L and the concentration R_{200b}/r_s of the subsamples as in Section 4.4. The upper (lower) triangles in each panel of Figure 9 represent the fitting results of b_L , and R_{200b}/r_s for the subsamples with 33% higher (lower) values of the amount of pseudo evolution at different redshifts. The figure shows that the secondary bias by the amount of pseudo evolution can be more prominent for the halos with smaller ν and all the subsamples with higher f_{pseudo} in this study tend to be of larger concentrations and reside in the environment with a greater linear bias than the full sample.

REFERENCES

- Allen, S. W., Evrard, A. E., & Mantz, A. B. 2011, Annual Review of Astronomy and Astrophysics, 49, 409
- Baldauf, T., Seljak, U., Desjacques, V., & McDonald, P. 2012, PhRvD, 86, 083540

- Behroozi, P. S., Wechsler, R. H., & Wu, H.-Y. 2013a, *ApJ*, 762, 109
- Behroozi, P. S., Wechsler, R. H., Wu, H.-Y., et al. 2013b, *ApJ*, 763, 18
- Bryan, G. L., & Norman, M. L. 1998, *ApJ*, 495, 80
- Bullock, J. S., Kolatt, T. S., Sigad, Y., et al. 2001, *MNRAS*, 321, 559
- Catelan, P., & Theuns, T. 1996, *MNRAS*, 282, 436
- Chue, C. Y. R., Dalal, N., & White, M. 2018, *Journal of Cosmology and Astro-Particle Physics*, 2018, 012
- Covone, G., Sereno, M., Kilbinger, M., & Cardone, V. F. 2014, *ApJ*, 784, L25
- Crocce, M., Pueblas, S., & Scoccimarro, R. 2006, *MNRAS*, 373, 369
- Cuesta, A. J., Prada, F., Klypin, A., & Moles, M. 2008, *MNRAS*, 389, 385
- Dalal, N., White, M., Bond, J. R., & Shirokov, A. 2008, *ApJ*, 687, 12
- De Boni, C., Serra, A. L., Diaferio, A., Giocoli, C., & Baldi, M. 2016, *ApJ*, 818, 188
- de Haan, T., Benson, B. A., Bleem, L. E., et al. 2016, *ApJ*, 832, 95
- Diemand, J., Kuhlen, M., & Madau, P. 2007, *ApJ*, 667, 859
- Diemer, B. 2017, *The Astrophysical Journal Supplement Series*, 231, 5
- Diemer, B., & Kravtsov, A. V. 2014, *ApJ*, 789, 1
- Diemer, B., More, S., & Kravtsov, A. V. 2013, *ApJ*, 766, 25
- Duffy, A. R., Schaye, J., Kay, S. T., et al. 2010, *MNRAS*, 405, 2161
- Faltenbacher, A., & White, S. D. M. 2010, *ApJ*, 708, 469
- Fedeli, C. 2012, *MNRAS*, 424, 1244
- Gao, L., & White, S. D. M. 2007, *MNRAS*, 377, L5
- Gunn, J. E., & Gott, III, J. R. 1972, *ApJ*, 176, 1
- Hahn, O., Porciani, C., Dekel, A., & Carollo, C. M. 2009, *MNRAS*, 398, 1742
- Hamana, T., Oguri, M., Shirasaki, M., & Sato, M. 2012, *MNRAS*, 425, 2287
- Hamana, T., Takada, M., & Yoshida, N. 2004, *MNRAS*, 350, 893
- Hayashi, E., & White, S. D. M. 2008, *MNRAS*, 388, 2
- Heavens, A., & Peacock, J. 1988, *MNRAS*, 232, 339
- Johnston, D. E., Sheldon, E. S., Wechsler, R. H., et al. 2007, *arXiv e-prints*, arXiv:0709.1159
- Lewis, A., Challinor, A., & Lasenby, A. 2000, *ApJ*, 538, 473
- Ludlow, A. D., Navarro, J. F., Boylan-Kolchin, M., et al. 2013, *MNRAS*, 432, 1103
- Madhavacheril, M. S., Battaglia, N., & Miyatake, H. 2017, *PhRvD*, 96, 103525
- Mantz, A. B., Allen, S. W., Morris, R. G., et al. 2014, *MNRAS*, 440, 2077
- Mao, Y.-Y., Zentner, A. R., & Wechsler, R. H. 2018, *MNRAS*, 474, 5143
- Medezinski, E., Battaglia, N., Umetsu, K., et al. 2018, *Publications of the Astronomical Society of Japan*, 70, S28
- Miyatake, H., Battaglia, N., Hilton, M., et al. 2019, *ApJ*, 875, 63
- Miyazaki, S., Oguri, M., Hamana, T., et al. 2018, *Publications of the Astronomical Society of Japan*, 70, S27
- More, S., Diemer, B., & Kravtsov, A. V. 2015, *ApJ*, 810, 36
- Murata, R., Nishimichi, T., Takada, M., et al. 2018, *ApJ*, 854, 120
- Navarro, J. F., Frenk, C. S., & White, S. D. M. 1997, *ApJ*, 490, 493
- Nishimichi, T., Shirata, A., Taruya, A., et al. 2009, *Publications of the Astronomical Society of Japan*, 61, 321
- Nishimichi, T., Takada, M., Takahashi, R., et al. 2018, *arXiv e-prints*, arXiv:1811.09504
- Oguri, M., & Takada, M. 2011, *PhRvD*, 83, 023008
- Okabe, N., Smith, G. P., Umetsu, K., Takada, M., & Futamase, T. 2013, *ApJ*, 769, L35
- Paranjape, A., Hahn, O., & Sheth, R. K. 2018, *MNRAS*, 476, 3631
- Planck Collaboration, Ade, P. A. R., Aghanim, N., et al. 2016a, *A&A*, 594, A24
- . 2016b, *A&A*, 594, A13
- Press, W. H., & Schechter, P. 1974, *ApJ*, 187, 425
- Press, W. H., Teukolsky, S. A., Vetterling, W. T., & Flannery, B. P. 1992, *Numerical recipes in FORTRAN. The art of scientific computing*
- Rozo, E., Wechsler, R. H., Rykoff, E. S., et al. 2010, *ApJ*, 708, 645
- Schaller, M., Frenk, C. S., Bower, R. G., et al. 2015, *MNRAS*, 451, 1247
- Shi, J., Wang, H., & Mo, H. J. 2015, *ApJ*, 807, 37
- Shirasaki, M., Hamana, T., & Yoshida, N. 2015, *MNRAS*, 453, 3043
- . 2016, *Publications of the Astronomical Society of Japan*, 68, 4
- Shirasaki, M., Lau, E. T., & Nagai, D. 2018, *MNRAS*, 477, 2804
- Simet, M., McClintock, T., Mandelbaum, R., et al. 2017, *MNRAS*, 466, 3103
- Springel, V. 2005, *MNRAS*, 364, 1105
- Takahashi, R., Sato, M., Nishimichi, T., Taruya, A., & Oguri, M. 2012, *ApJ*, 761, 152
- Tinker, J., Kravtsov, A. V., Klypin, A., et al. 2008, *ApJ*, 688, 709

Umetsu, K., Broadhurst, T., Zitrin, A., et al. 2011, *ApJ*,
738, 41

Valageas, P., & Nishimichi, T. 2011, *A&A*, 527, A87

Vikhlinin, A., Kravtsov, A. V., Burenin, R. A., et al. 2009,
ApJ, 692, 1060

Wang, H., Mo, H. J., Jing, Y. P., Yang, X., & Wang, Y.
2011, *MNRAS*, 413, 1973

Wechsler, R. H., Bullock, J. S., Primack, J. R., Kravtsov,
A. V., & Dekel, A. 2002, *ApJ*, 568, 52

Wechsler, R. H., Zentner, A. R., Bullock, J. S., Kravtsov,
A. V., & Allgood, B. 2006, *ApJ*, 652, 71

Wetzel, A. R., & Nagai, D. 2015, *ApJ*, 808, 40

Zemp, M. 2014, *ApJ*, 792, 124